# Magma ascent at floor-fractured craters diagnoses the lithospheric stress state on the Moon

Chloé Michaut

*Laboratoire de Géologie de Lyon, Université de Lyon, Ecole Normale Supérieure de Lyon, Université Lyon-1, CNRS, UMR 5276, 46 allée d'Italie, F-69364, Lyon, France*

Virginie Pinel

*Université Grenoble Alpes, Univ. Savoie Mont Blanc, CNRS, IRD, IFSTTAR, ISTerre, 38000 Grenoble, France*

Francesco Maccaferri

*German Research Centre for Geoscience (GFZ), Telegrafenberg, 14473, Potsdam, Germany and Istituto Nazionale di Geofisica e Vulcanologia INGV, Osservatorio Vesuviano, Napoli, Italy*

**Abstract**

On the Moon, floor-fractured craters (FFCs) present evidence of horizontal crater-centred magmatic intrusions. Crater floor uplift and moat formation indicate that these sill intrusions occur at shallow depths ($< 10$ km). While a recent study has demonstrated that magma ascent below FFCs and mare-filled craters was triggered by crater unloading, the mechanism leading to the emplacement of shallow sills is still poorly understood. Here we show that the local stress field due to crater unloading is also responsible for the horizontalisation of the magma flow leading to sill-like intrusions. On Earth, caldera formation has been shown to similarly affect magma trajectories, inducing the formation of a sill-shaped storage zone. Magma ascent to shallow depths below FFCs was however made possible because of a regional tensional stress caused by mare loading on the lunar lithosphere. We show that the tensional stress generated by elastic lithosphere deformation

*Preprint submitted to Earth Planet. Sc. Lett.* *March 8, 2020*

caused by mare loading combined to the local crater stress field can explain the distribution of FFCs on the Moon, with the smallest FFCs being located over a larger distance range from the mare. In particular, FFCs distribution around Oceanus Procellarum is consistent with an average load thickness of $\sim$1 km. This study suggests that magma trajectory in the crust of terrestrial planets can provide a diagnostic of the lithospheric structure and state of stress.

*Keywords:*
magma intrusion, crustal stress field, magma path, floor-fractured crater, lunar mare

---

## 1. Introduction

In the crust of terrestrial planets, magma transport occurs by magma flow through induced fractures referred to as dykes or sills depending on their orientation relative to lithologic layers or verticality. Observations show that horizontal sills and laccoliths on Earth are fed by vertical dykes and inversely, dykes are fed by horizontal sills in large sill complexes. (Cartwright and Moller Hansen, 2006; Muirhead et al., 2012; Richardson et al., 2015): intrusions thus deviate from their initial orientations. The presence of inherited structures or the reaching of a neutral buoyancy zone are often advocated to explain deviations in magma paths (Menand, 2011). Recently, studies on the trajectory of magma in the Earth's crust have shed light on the crucial influence of the stress field on magma trajectory and its ability to reach the surface (Pinel et al., 2017; Corbi et al., 2015; Maccaferri et al., 2014). Below a volcanic edifice, the induced compressive stress opposes to magma ascent, allowing only for the ascent of the least dense and thus most differentiated magmas (Pinel and Jaupart, 2000). Providing the magma driving force (overpressure) is weak, the crustal stress field may exert a strong control on the trajectories of magma. Magmatic dykes tend to open in the direction of least compressive stress ($\sigma_3$) (Anderson, 1951; Nakamura, 1977). Analog experiments (Watanabe et al., 2002; Corbi et al., 2016) and numerical models (Mériaux and Lister, 2002; Maccaferri et al., 2011) indeed show that dyke paths are more influenced by the local stress if the magma driving force is weak.

On the Moon, floor-fractured craters (FFCs) are impact craters that were modified after their formation. Compared to non-modified craters, they show fractured and uplifted floors that are believed to result from crater-centred horizontal sill or laccolith intrusions (Schultz, 1976a; Wichman and Schultz, 1995; Jozwiak et al., 2012; Thorey and Michaut, 2014). The magma feeding these intrusions must have been transported through vertical dykes and then turned into a horizontal sill at a shallow depth to explain the observed floor uplift (Jozwiak et al., 2015; Wilson and Head, 2017). Deviation from the vertical has previously been explained by the presence of a highly brecciated zone caused by the impact. Schultz (1976a) proposed that the magma reaching the breccia lens filled the subhorizontal inherited fractures forming a sill while the impact melt sheets welded the crater floor, leading to cohesive floor deformation and uplift. Jozwiak et al. (2012, 2015) alternatively proposed that the vertical ascent of magma was halted because of the low density of the brecciated zone. The impact crater topography naturally results from crustal material redistribution, which can be described by surface unloading forces. The elastic stresses underneath impact craters have been studied by Melosh (1976) but the effect of unloading forces on the principal stresses direction beneath a crater has never been considered in the context of FFC formation. On Earth, it has been shown that unloading forces due to rift valleys and calderas formation would affect magma pathways (Maccaferri et al., 2014; Corbi et al., 2015). In fact, below a surface unloading, the direction of $\sigma_3$ is often vertical, favouring the formation of horizontal sills (Corbi et al., 2015; Pinel et al., 2017) in case the magma driving force is weak.

The lunar Highlands, where many FFCs are present, are composed of ancient, highly porous, anorthositic rocks (Wood et al., 1970). Analysis of GRAIL's gravity data show that this ancient primary crust has a low average density of $\sim 2550$ kg m$^{-3}$ (Wieczorek et al., 2013). The buoyancy of basaltic magma in such a low density crust is very limited, therefore, the resulting magma overpressure may be small enough for magma trajectories to be sensitive to the local stress field at the time of intrusion.

Michaut and Pinel (2018) have recently shown that crater unloading can trigger magma ascent in the lunar crust, the decompression of the encasing rocks providing a relative overpressure to the magma that was ponding at depth. Observations indeed show that for large craters on a thin crust, magma erupted on the floor of mare-filled craters and of some FFCs, suggesting that the overpressure provided by the unloading was large enough for the magma to reach the surface. However, for smaller craters or a thicker crust, crater floor uplift is observed suggesting that the overpressure was too small for the magma to reach the surface (Michaut and Pinel, 2018). Here we show that, below such craters, the local stress field due to crater unloading is the cause of magma path deviation from a vertical dyke to a horizontal sill. This sill formation is however expected to occur close to the crust base, preventing any further ascent. It follows that the emplacement of shallow intrusions cannot be explained considering only the crater unloading effect. We demonstrate that the presence of dense basaltic maria and mascons in

Table 1: Defining characteristics of each classes of floor-fractured crater, after Schultz (1976a) and Jozwiak et al. (2012).

| Crater Class | Characteristics |
|---|---|
| 1 | Deep, fractured floors, mare material along walls |
| 2 | Well defined wall scarp, uplifted central region / convex up floor profile, concentric fractures |
| 3 | Wide U-moat between wall scarp and uplifted crater interior, radial and polygonal fractures |
| 4 a,b,c | V-shaped moat with a convex up floor profile to hummocky interior |
| 5 | Degraded walls and fractured floors |
| 6 | Mare-flooded interiors, concentric fracture near wall |

the nearby region added an important contribution to the lithospheric stress field, allowing for a vertical magma ascent up to shallow depths. By taking into account maria-induced stress, we explain the size and spatial distribution of FFCs around the lunar maria and use it to constrain mare thicknesses.

## 2. Observations on lunar floor-fractured craters

FFCs are craters presenting radial and concentric floor fractures. Their floors are generally uplifted compared to non-modified craters of the same size. Schultz (1976a), and lately Jozwiak et al. (2012), proposed a classification into six different FFC classes on the Moon based on crater floor morphologies and appearances (Table 1). Crater-centred intrusion of basaltic magma is believed to be the cause of floor deformation and uplift (Schultz, 1976a; Jozwiak et al., 2012; Thorey et al., 2015). In fact, volcanic deposits are often present within these craters, and theoretical models for the dynamics of crater-centred horizontal intrusions well explains the diversity of crater floor appearances (Thorey and Michaut, 2014). Furthermore, FFCs are distributed around basaltic maria and mascons (Figure 1), at distances reaching one to two thousands of kilometers from these maria. Craters of Class 4, although smaller in size than those of other classes, occur over a greater distance range from the maria, deeper into the Highlands (green dots on Figure 1) (Schultz, 1976a).

Craters of Classes 2, 3 and 4 present an uplifted floor (dots on Figure 1), that appears either convex up or flat with a circular moat bordering the inner side of the crater wall (Table 1). Such floor appearances are characteristics of large sill-like intrusions (with opening of up to several hundred meters to a few kilometers) at shallow depth (Thorey and Michaut, 2014) and hence of a strong deviation of the magma paths from vertical feeding dikes to horizontal sills occurring lately in the ascent. For such craters, the effective overpressure provided to the magma by the crater unloading was not large enough to allow for eruption and magma got trapped at depth (Michaut and Pinel, 2018). Thus, the magma driving pressure was supposedly small and the magma was likely sensitive to the lithospheric stress state (Watanabe et al., 2002).

Craters of Class 1 show fractures and mare patches along the crater wall but their floors have not been uplifted. Such characteristics do not point to the presence of a large sill-like intrusion. Craters of Class 6 are completely flooded and it is thus not possible to know if a large-volume horizontal intrusion is present at depth. Craters of Class 1 and 6 are generally large craters (Jozwiak et al., 2012) on a relatively thin crust such that the crater unloading generally provided enough effective overpressure for the magma to reach the surface (see Figure 3 of Michaut and Pinel (2018)). For those two classes, the driving pressure was probably too large for the magma to be very sensitive to the lithospheric state of stress (Michaut and Pinel, 2018).

Craters of class 5 are old and degraded (Jozwiak et al., 2012) and are not considered in our analysis.

We assume that the initial vertical ascent of the magma was triggered by the unloading caused by the excavation of material following an impact (Michaut and Pinel, 2018). For a small driving pressure, the magma path is likely to be controlled by the lithospheric stress state (Watanabe et al., 2002). We model the stress state below lunar FFCs to quantitatively estimate if and under which conditions it may explain magma flow horizontalization and magma storage at shallow depth. We thus limit our analysis to FFCs of Class 2, 3 and 4 that show evidence of a strong deviation of the magma from the vertical. We do not account for FFCs in the South Pole Aitken Basin (SPA) (Figure 1). GRAIL's gravity data indeed show regional variations of the crust density of $\pm 250$ kg m$^{-3}$, primarily between the highlands and the SPA (where the crust is denser), which tend to increase the magma driving pressure and affects its crustal trajectory.

## 3. Stress model

We model the local stress field acting beneath a crater taking into account two main contributions: i) the unloading forces due to crater formation, and ii) the loading due to the presence of mare and mascons. The total stress field is obtained by superposing these two stress fields.

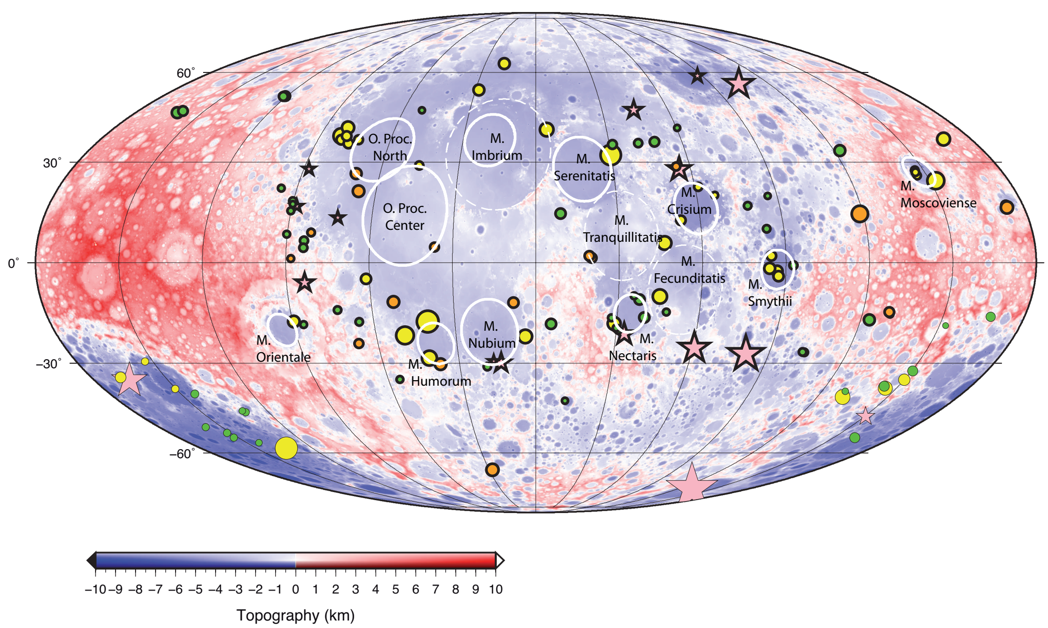


Figure 1: Distribution of lunar floor fractured craters that show an uplifted convex floor (Class 2, orange circles, Class 4 green circles) or an uplifted flat floor (Class 3, yellow circles) or, in pink stars, that show a flooded interior (Class 1) or mare material on their floor (Class 6). The crater distribution is superimposed on the surface topography with Highlands appearing in red. Symbol size is proportional to crater size. Bold symbols represents craters that are used in the following analysis while thin symbols, located in the South Polar Aitken basin area, are not considered. Mare positions and extensions as listed in Table 2 are also represented.

### 3.1. Local stress due to crater unloading

To calculate the local stress induced by a crater unloading, we follow Michaut and Pinel (2018) and treat the crater depression as a negative load on an elastic medium. A bowl-shape axisymmetric crater of radius $R$ results in a stress $\sigma_{zz}^C(z = 0)$:

$$\sigma_{zz}^C(0 \leq r \leq R, z = 0) = -\rho_c g h_0 \left(1 - \frac{r^2}{R^2}\right) \tag{1}$$

where tensile stresses are assumed negative, $\rho_c$ is crustal density, $g$ gravity, $r$ radial coordinate, $z$ is the depth defined with respect to the ground plane, and $h_0$ the maximum crater depth, expressed as a function of the crater radius following Thorey et al. (2015):

$$h_0 = 540 \times (2 \times R \times 10^{-3})^{0.44} \tag{2}$$

where $h_0$ and $R$ are in meters. We neglect the loading forces associated with the crater rim and central peak topography. The stress field caused by the unloading is determined from the equations for linear elasticity which we solved using the Finite Element Method (COMSOL software) for an elastic plate of finite thickness $T_e$, and for a semi-infinite medium. The analytical solutions of Pinel et al. (2017) for the displacement induced by the loading of a thick elastic plate on an inviscid medium have been used to validate our numerical solutions. Results for large plate thicknesses compared to crater radius tend to the analytical results for a semi-infinite medium (Sneddon, 1951). The vertical profile of radial, tangential and vertical stresses in a semi-infinite elastic medium of Poisson's ratio $\nu$ at the axis ($r = 0$) of a bowl-shape load of radius $R$ are respectively given by Michaut and Pinel (2018):

$$
\begin{aligned}
\sigma_{rr}^{C,\infty}(z) &= -\frac{\rho_c g h_0}{R^2}\left((1+2\nu)\frac{R^2}{2} - 2(1+\nu)z\sqrt{R^2+z^2} + (3+2\nu)z^2 - \frac{z^3}{\sqrt{R^2+z^2}}\right) \\
\sigma_{\theta\theta}^{C,\infty}(z) &= \sigma_{rr}^{C,\infty}(z) \\
\sigma_{zz}^{C,\infty}(z) &= -\frac{2\rho_c g h_0}{R^2}\left(\frac{R^2}{2} + \frac{z^3}{\sqrt{R^2+z^2}} - z^2\right)
\end{aligned}
$$

where the geometry is axisymmetric with respect to $z$, the vertical coordinate oriented downwards, and equal to zero at the surface. The exponent $\infty$ denotes a semi-infinite medium. At depth, the horizontal and vertical stresses scale with the surface unloading and decrease over a characteristic depth similar to the crater radius.

At the unloading axis, the horizontal stress is such that $\sigma_{rr}^{C}(0,z) > \sigma_{zz}^{C}(0,z)$. Therefore the direction of maximum compressive stress $\sigma_1$ is horizontal (Figure 2 top) while the minimum compressive stress $\sigma_3$ is vertical, and a magma intrusion with small overpressure would tend to form deep horizontal sills below craters. Floor appearance at FFCs of Class 2, 3 and 4 are indeed consistent with horizontal crater-centred intrusions (Thorey and Michaut, 2014) but at shallow depths ($< 10$ km), allowing for roof uplift.

### *3.2. Local stress due to unloading in a regional extension*

If a pre-existing regional stress field is present, due to the presence of mare and mascons, the direction of maximum compressive stress below a crater would result from the superposition of both the mare or mascon loading and the crater unloading. Since the mare loads are much larger in radius than the elastic lithosphere thickness, the vertical stresses can be neglected. If the regional horizontal state of stress is compressive, the maximum compressive stress along the $z$ axis

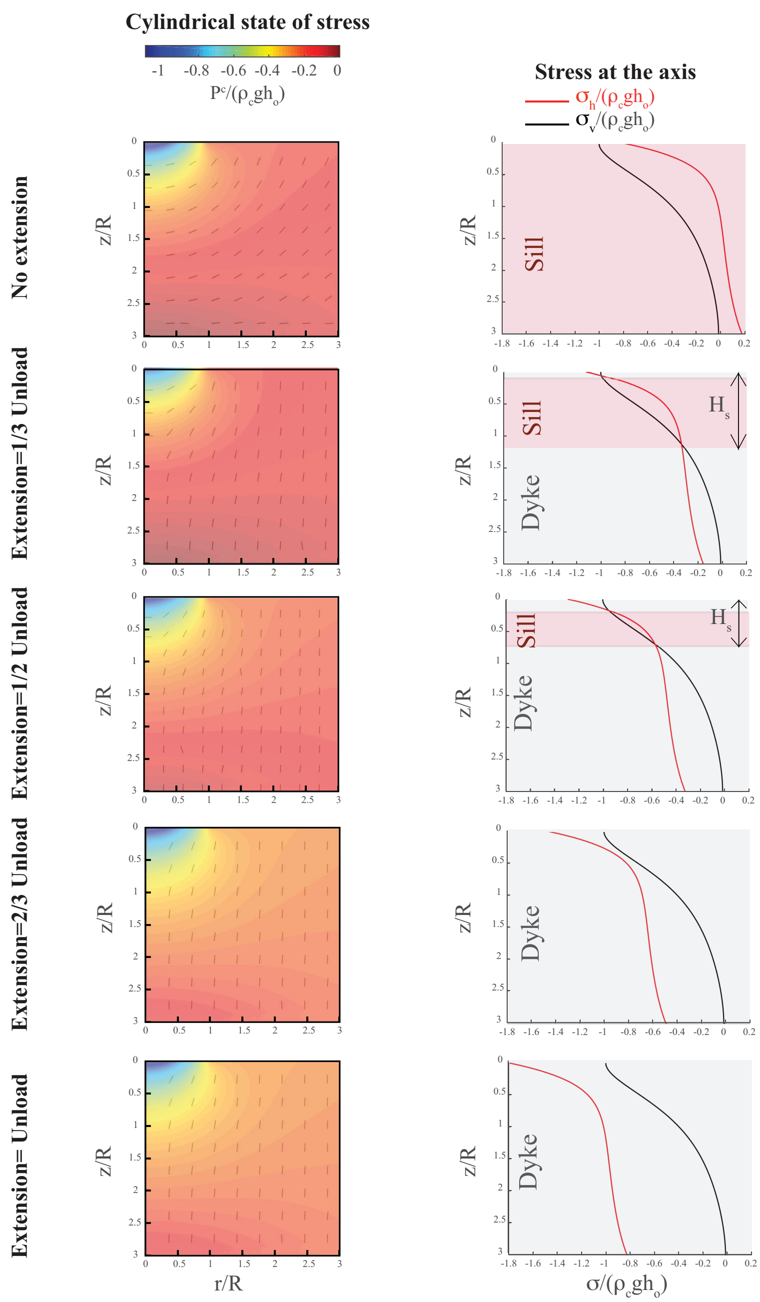


Figure 2: Left, three-dimensional axisymmetric pressure field (colour scale) and direction of maximum compressive stress $\sigma_1$ (dashes) below a bowl-shape surface unloading of radius $R$ (equation 1) in an elastic plate of thickness $T_e = 3R$ and for different pre-existing regional stress fields (top to bottom). The pre-existing regional radial stress and tangential stress $\sigma_{\theta\theta}^{ext} = \sigma_{rr}^{ext} = \sigma_H^{ext}$ are homogenous vertically and increase progressively in tension from top, where it is $\sigma_H^{ext} = 0$, to bottom, where the horizontal stress in tension is equal to the unload $\sigma_H^{ext} = -\rho_c g h_0$. Right, for each pre-existing regional stress field, the vertical profiles of radial (red) and vertical (black) stress are shown at the axis of the depression. The depth $H_s$ where the maximum compressive stress becomes horizontal is indicated. Results are for $\nu = 0.2$, $E = 10$ GPa, $g = 1.62$ ms$^{-2}$,

remains horizontal. However, if the regional stress displays uniform horizontal extension, depending on the magnitude of $\sigma_H^{ext} < 0$, the maximum compressive stress may become vertical below a given depth $H_s$ for which $\sigma_H(z) < \sigma_{zz}(z)$ (Figure 2). This would allow for vertical dikes deeper than $H_s$, and horizontal sills above $H_s$. The transition depth $H_s$ progressively becomes shallower as extension increases (Figure 2). Actually, mare loading generates a combination of both membrane stresses, homogenous with depth, and bending stresses, linearly varying with depth, whose effects are considered next.

When the regional tensional stress is such that $\sigma_H^{ext} \leq -0.6\rho_c g h_0$, the maximum compressive stress is vertical over the whole plate thickness (Figure 2, bottom). This threshold can be derived from the analytical solution for the semi-infinite medium and is independent of Young's modulus value. In such a case, crater unloading would provide the driving overpressure for magma to rise through the crust but no horizontal deflection would occur.

Hence, below a relatively small crater or in a thick low density crust (as for FFCs of classes 2, 3 and 4), the magma can ascend up to shallow depths ($< 10$ km) and then turn into a horizontal sill if the tensional stress field amplitude is $\lesssim 0.6\rho_c g h_0$, so that the crater stress field, which favours horizontal sills, dominates over extension at shallow depth.

### *3.3. Pre-existing regional stress field due to mascon and mare load*

FFCs are distributed around the main maria suggesting either that lunar magmas were produced only in this specific area due to its enrichement in radioelements (Laneuville et al., 2013) or that the geological context associated to impact basins favoured magma ascent at their periphery because their formation has generated pre-existing fractures and magma pathways (Schultz, 1976a) or because

Table 2: Mare characteristics, after https://planetarynames.wr.usgs.gov, International Astronomical Union (IAU), Working Group for Planetary System Nomenclature for most mare or Neumann et al. (2015). For simplicity, Oceanus Procellarum (OP) is here modelled as two large circular loads named OP Centre and OP North.

| Mare | North Latitude | East Longitude | Radius (km) |
|---|---|---|---|
| Oceanus Procellarum Centre | 14 | 312 | 450 |
| Oceanus Procellarum North | 34 | 298 | 300 |
| Mare Serenitatis | 28 | 18 | 300 |
| Mare Crisium | 16 | 59 | 230 |
| Mare Smythii | -2 | 87 | 177 |
| Mare Moscoviense | 27 | 148 | 138 |
| Mare Orientale | -20 | 266 | 147 |
| Mare Humorum | -24 | 322 | 190 |
| Mare Nubium | -21 | 343 | 300 |
| Mare Nectaris | -15 | 35 | 170 |
| Mascon Imbrium | 37 | 341 | 250 |
| Mare Imbrium | 33 | 345 | 530 |
| Mare Tranquillitatis | 8 | 31 | 400 |
| Mare Fecunditatis | -8 | 54 | 400 |

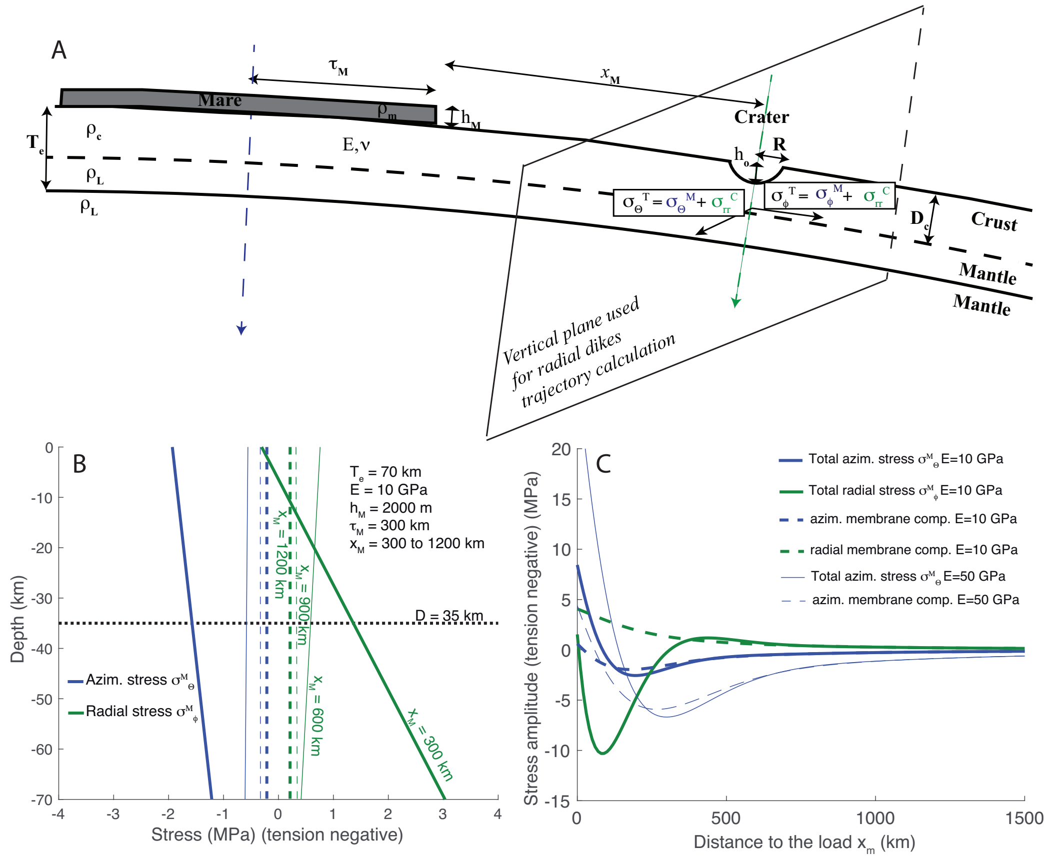


Figure 3: A: Stress field components ($\sigma_\Theta^T$ and $\sigma_\Phi^T$) in the elastic lithosphere at the axis of a bowl-shape crater of radius $R$ and depth $h_o$ at a distance $\mathrm{x}_M$ from a load of radius $\tau_M$, thickness $h_M$ and density $\rho_M$. This stress field is the summation of the crater unloading contribution $\sigma_{rr}^C = \sigma_{\theta\theta}^C$ and the mare/mascon loading one $\sigma_\Theta^M$ and $\sigma_\Phi^M$. Note that the elastic lithosphere contains a lithological boundary at depth $D_c$ separating the crust and the mantle. Bottom: Horizontal azimuthal (blue) $\sigma_\Theta^M$ and radial (green) $\sigma_\Phi^M$ stresses (with respect to load center) caused by a circular load as a function of depth for four different distances from the load $\mathrm{x}_M = 300, 600, 900, 1200$ km indicated on the graphs (same lines but two colours for azimuthal and radial stress, B) or at the surface as a function of distance from the load $\mathrm{x}_M$ (C). We use $T_e = 70$ km, $E = 10 - 50$ GPa, $\nu = 0.2$, $h_M = 2000$ m, $\rho_M = 3100$ kg m$^{-3}$, $\rho_L = 3400$ kg m$^{-3}$, $\rho_c = 2500$ kg m$^{-3}$ and $\tau_M = 300$ km. On $C$, azimuthal stresses are also indicated in the case $E = 50$ GPa ; membrane stress components (homogenous with depth) dominate at distances $\geq 3\Lambda$ from the load.

they induce tensional stresses by lithosphere loading. McGovern and Litherland (2011) suggested indeed that lava filling of large circular basins on the Moon created a specific regional stress state that promoted magma ascent through vertical dikes in annular regions at the periphery of these large circular loads. We examine the possibility, following McGovern and Litherland (2011) and Thomas et al. (2015), that lithosphere loading by mascons and mare weight has induced a pre-existing regional extensive stress on their periphery, favouring magma ascent through vertical dikes to shallower depths.

We model the regional lithostatic stress state $\sigma^M$ induced by a mare load using the analytical solution for azimuthal and radial stress $\sigma_\Theta^M$ and $\sigma_\Phi^M$ around a circular load (Brotchie, 1971; Solomon and Head, 1979; Freed et al., 2001). We account for bending and membrane stresses in an elastic spherical shell of thickness $T_e$ (see Appendix).

The amplitude of regional horizontal stresses are sensitive to the load properties: assuming a circular mare load, they increase with mare radius $\tau_M$ (Figure 3) and are directly proportional to its surface mass or load thickness $h_M$, for a given load density. Bending stresses vary linearly with depth and dominates over membrane stresses closer to the mare over a width that is equal to a few times the flexural wavelength of the elastic lithosphere $\Lambda = \left(\frac{ET_e^3}{(1-\nu^2)\rho_L g}\right)^{1/4}$, where $E$ and $\nu$ are the lithosphere Young's modulus and Poisson's ratio, $\rho_L$ is lithosphere density. For $T_e = 70$ km, $E = 10$ GPa, $\Lambda \approx 85$ km and bending stresses dominates over a width of $\sim 0 - 250$ km (Figure 3). Very close to the load, bending causes tensional radial stresses close to the surface and tensional azimuthal stresses at depth ($\sim 0 - 250$ km from the load on Figure 3C) and inversely a little farther away ($\sim 250 - 350$ km from the load on Figure 3C). Membrane stress components are constant with depth in the lithosphere and are dominant in the far field ($>$ 200-300 km from the load, Figure 3C). Radial membrane stresses are in compression; on the contrary, azimuthal membrane stresses are in tension (Figure 3, B and C), favouring radial fracture opening. The azimuthal membrane stress decreases from a small positive value (compression) at the load border to a minimum negative value (maximum in tension) at $\sim 200$ km from the load for the example of Figure 3C; it then slowly increases back towards zero at larger distances. The azimuthal membrane stress caused by mare loading could have favoured radial dyke opening over distances larger than a thousand kilometers from the load. However, it was not the cause of magma ascent below FFCs, since, in that case, the magma would have reached the surface everywhere and not formed crater-centred intrusions.

### *3.4. Total stress field*

To compute the total stress field acting beneath the crater, we superpose the local stress field induced by the crater, estimated using COMSOL numerical calculations (Figure 2 top), and the pre-existing regional stress field caused by a circular mare load on an elastic spherical lithosphere of finite thickness $T_e$ (Figure 3). To examine a wide range of parameters, we estimate the stress field at the crater axis and look for solutions favourable to shallow crater-centred sill intrusions. In terms of stress state, solutions should allow for the formation of a dike (radial or concentric relative to mare geometry) at the base of the crust $D_c$, hence a horizontal least compressive stress at $z = D_c$, as well as the formation of a sill at shallower depths in the crust, i.e. a vertical least compressive stress at a depth $z$ such that $0 < z < D_c$ (Figure 4A). The magma is assumed buoyant in the lithospheric mantle where its path is not affected by the stress field. Solutions depend on crater radius $R$, lithosphere thickness $T_e$, distance to load $\mathrm{x}_M$, load thickness

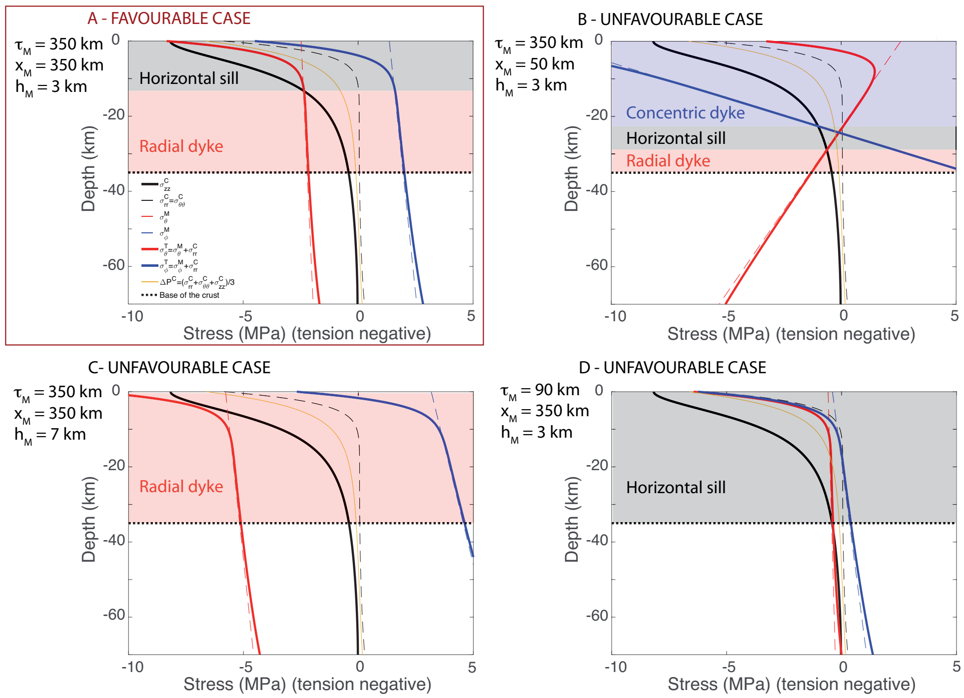


Figure 4: Different cases of stress field at the axis of an unloading as a function of depth for $T_e = 70$ km, $E = 10$ GPa, $R = 10$ km, and for different indicated values of load radius $\tau_M$, distance to mare border $\mathrm{x}_M$ and load thickness $h_M$. Black solid line: vertical stress, only due to crater unloading. Red solid line: total azimuthal stress with respect to mare centre, sum of the azimuthal stress due to mare load (red dashed line) and horizontal stress due to crater unloading (black dashed line). Blue solid line: total radial stress with respect to mare centre, sum of the radial stress due to mare load (blue dashed line) and horizontal stress due to crater unloading (black dashed line). Yellow solid line: pressure perturbation due to unloading. An arbitrary crustal thickness of 35 km is illustrated by a horizontal dotted line. Only the stress state in A allows for vertical magma ascent followed by flow horizontalization at a shallow depth. In B, vertical dike is favoured at the base of the crust followed by a sill at shallower depths but bending stresses are so important close to the load ($\mathrm{x}_M = 50$ km) that the total tectonic stress gradient opposes to magma ascent and cannot be compensated by the driving pressure due to unloading. In C, extension induced by mare loading dominates preventing sill formation whereas in D it is too small to enable dike formation at the crust base.

$h_M$, load radius $\tau_M$ as well as Young's modulus value. Depending on the values of these parameters we obtain four different stress regimes (Figure 4, panels A to D), which would cause different propagations of magmatic intrusions nucleated at the crust base below the crater.

If the amplitude of the azimuthal membrane stress is larger than $0.6\rho_c g h_0$, it dominates over the crater stress field, which would cause magma ascent in radial dikes and eruption within the crater floor (Figures 4C and 2 bottom). Such a scenario would not explain observed floor uplift at FFCs of Classes 2, 3 and 4. On the contrary, if the membrane stress is too small, such that a vertical dyke is not allowed at the base of the crust, the magma would form deep horizontal intrusions, which would not explain floor deformations either (Figure 4D).

Close to the load ($x_M \lesssim 200$ km), bending stress dominates over membrane stress and might be such that a vertical dike is favoured at the crust base followed by a horizontal sill within the crust (Figure 4B). However, in that case, the vertical stress gradient $d\sigma^H/dz$ is positive and opposes to magma ascent (the azimuthal pre-existing stress largely increases with height, red curve on Figure 4B). The overpressure $P^C$ provided by crater unloading at $z = D_c$ allows for magma ascent to shallow depths ($< 10$ km) only if $P^C$ counteracts the positive vertical gradient in total stress up to 10 km depth, or up to the depth at which the vertical gradient in total stress reverses ($z^{\theta\phi} > 10$ km) favouring magma ascent:

$$\begin{aligned} |P^C(z = D_c)| &\geq \sigma^T_\Phi(z = max(z^{10}, z^{\Theta\Phi})) - \sigma^T_\Phi(z = D_c) \quad \text{if} \quad \sigma_3(D_c) = \sigma_\Phi(D_c) \\ |P^C(z = D_c)| &\geq \sigma^T_\Theta(z = max(z^{10}, z^{\Theta\Phi})) - \sigma^T_\Theta(z = D_c) \quad \text{if} \quad \sigma_3(D_c) = \sigma_\Theta(D_c) \end{aligned} \tag{3}$$

where $\Theta$ and $\Phi$ are respectively the azimuthal and radial coordinates relative to the load centre, $\sigma_3$ the least compressive stress, $\sigma_{\Phi}^T = \sigma_{\Phi}^M + \sigma_{rr}^C$ and $\sigma_{\Theta}^T = \sigma_{\Theta}^M + \sigma_{rr}^C$, where $\sigma^M$ is the stress generated by mascon/mare loading on the lithosphere and $\sigma^C$ the stress perturbation due to crater unload.

## 4. Results

### *4.1. Conditions favourable to shallow crater-centred magmatism*

For a given load radius, lithosphere elastic thickness and Young's modulus value, we look for solutions in terms of crater radius $R$, load thickness $h_M$ and distance to load $\mathrm{x}_M$ that would favour: i) a vertical dike at the crust base, ii) a dike to sill transition within the crust as well as iii) an effective overpressure that would drive magma up to shallow depths $\leq 10$ km (Equations 3).

For distances $\gtrsim$ 200-300 km, membrane stresses are dominant. Results show that as the mare thickness increases, the condition for having FFCs are met at increasing distances from the mare, and within a wider range. This result stands given a fixed load radius, crater radius and lithosphere thickness (Figure 5). When the load is too thick (for instance for $h_M > 4000$ m for $R = 10$ km, $T_e = 70$ km, $E = 10$ GPa and $\tau_M = 350$ km), azimuthal membrane stresses close to the load (at $\mathrm{x}_M \leq 200 - 300$ km) become larger than $0.6\rho_c g h_0$ and dominate over the local stress due to crater unloading (Figures 4C and 5). Far away from the load, membrane stresses become too small and vertical dikes cannot form at the base of the crust leading to deep sill intrusions (Figures 4 and 5).

At distances $\lesssim 200$ km to the mare, bending stresses are dominant and tectonic stresses tend to oppose to magma ascent. For the magma to ascend to shallow depths, the overpressure due to crater unloading has to compensate for the positive tectonic stress gradient. This is only possible if load thicknesses are sufficiently small. As the crater radius, and hence the induced overpressure, increases, the maximum possible load thicknesses slowly increases for distances $\lesssim 200$ km (Figure 5).

Our results show that, for a given mare thickness and radius, the smaller the crater radius, the easier it is for membrane stress to compensate for the vertical extension at depth caused by crater unloading. Therefore, shallow magmatism can occur below the crater at increasing distance from the mare (Figure 5) for a given load thickness and radius. As a result, shallow horizontal intrusions beneath small craters ($R < 10$ km) are likely to occur over a larger range of distances from the mare. Instead, shallow intrusions below large craters ($R > 20$ km) should only occur close to the mare (Figure 5).

Indeed Schultz (1976a) noted that small FFCs are found deep into the Highlands. To quantify this observation, we calculate the distance of each FFC to its closest and second closest mare by considering the main maria and assuming circular mare loads with a given centre and radius (see Table 2, Figure 1). Such a geometry is certainly simplified, in particular for Oceanus Procellarum (OP) that represents a broad positive gravity anomaly. But the 3D loading geometry is more difficult to represent. Mare Orientale is also associated to a more complex gravity signature, with a central gravity high encircled by a low gravity annulus itself surrounded by a broader gravity high region, which might be important to consider in the interpretation of individual FFC. Given that membrane stress plays over a large distance from the mare, it may also happen that the mare which is responsible for magma ascent is not the closest to the crater. However, our simplified model allows to obtain first-order quantitative results, and test our assumptions.

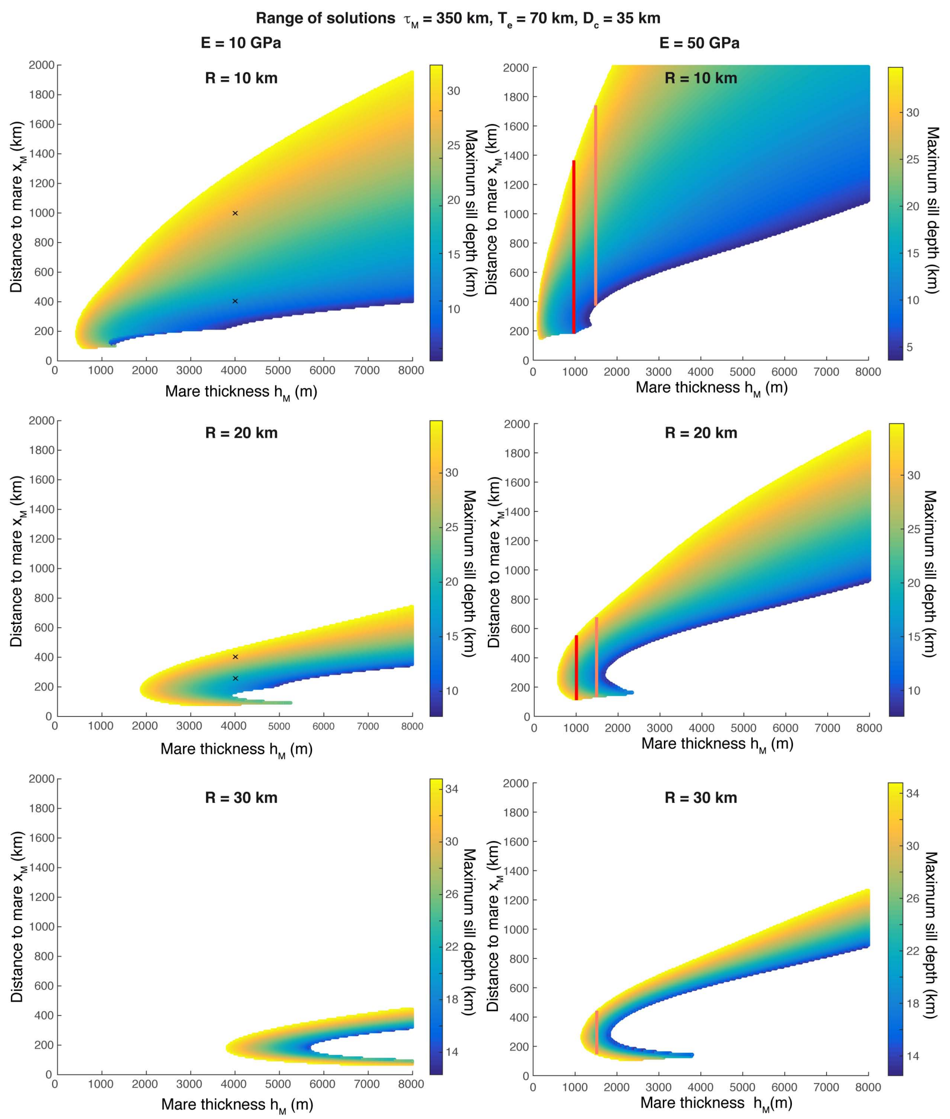


Figure 5: Range of possible solutions (coloured area) in terms of distance to mare load $x_M$ and mare thickness $h_M$ for a shallow magma intrusion to occur below a crater for different crater radius of 10 (top), 20 (middle) and 30 km (bottom), for a load radius $\tau_M = 350$ km, an elastic lithosphere thickness $T_e = 70$ km and a crustal thickness $D_c = 35$ km and using $E = 10$ GPa (left), or $E = 50$ GPa (right). $\nu = 0.2$, $g = 1.62$ ms$^{-2}$ and $\rho_L = 3400$ kg.m$^{-3}$, $\rho_c = 2500$ kg m$^{-3}$, $\rho_M = 3100$ kg m$^{-3}$. The maximum sill depth is the maximum depth at which the minimum compressive stress is vertical at the crater axis, thus assuming that the magma trajectory follows $\sigma_1$. The range of distances indicated in red for $h_M = 1000$ m and orange for $h_M = 1500$ m for $E = 50$ GPa correspond to the ones indicated on Figure 6A. Crosses on the left ($E = 10$ GPa) indicate the distance, mare load and crater radius used to calculate the stress state necessary to 2D simulations of Figure 7.

Results show that the range of observed distance to the mare indeed decreases as the crater radius increases: while small craters of radius $\sim 10$ km are found up to 1200 km away from a mare side, larger craters of $\sim 30$ km are found within a few hundreds of km from the maria (Figure 6A). A linear regression with negative slope fits FFCs radii as a function of their distance from the closest maria (Figure 6). Distances are considered with an error $\Delta x_M = \pm 100$ km. Considering or not Mare Tranquillitatis, Fecunditatis and the whole extent of Mare Imbrium do not significantly change the results (Figure 1), suggesting that these maria were not important actors for the occurrence of shallow magmatism below craters.

Figure 5 also shows the depth at which the minimum compressive stress turn from horizontal to vertical. In case the magma trajectory exactly follows $\sigma_1$, this would indicate a dyke to sill transition. These depths might be quite large, in particular far from the load. However, depending on the trade-off between the magnitude of the regional stress and the magma driving force, intrusions may display a delayed deflexion towards the direction of $\sigma_1$ (Watanabe et al., 2002; Menand et al., 2010), which would validate the whole possible range of solutions of Figure 5. This assumption is tested in the following section.

### *4.2. Results from dike propagation model*

In our analysis, we assumed that buoyancy and overpressure were small enough for the magma to exactly follow the direction of the maximum compressive stress. This approach has allowed us to look for solutions over a wide range of parameters in terms of load characteristics and distance from the mare. In order to validate these results, we make use of a 2D boundary element (BE) model to simulate the trajectory of a magmatic dike propagating within the crust (Maccaferri et al., 2011). Results from the BE model for dike propagation allow us to quantify

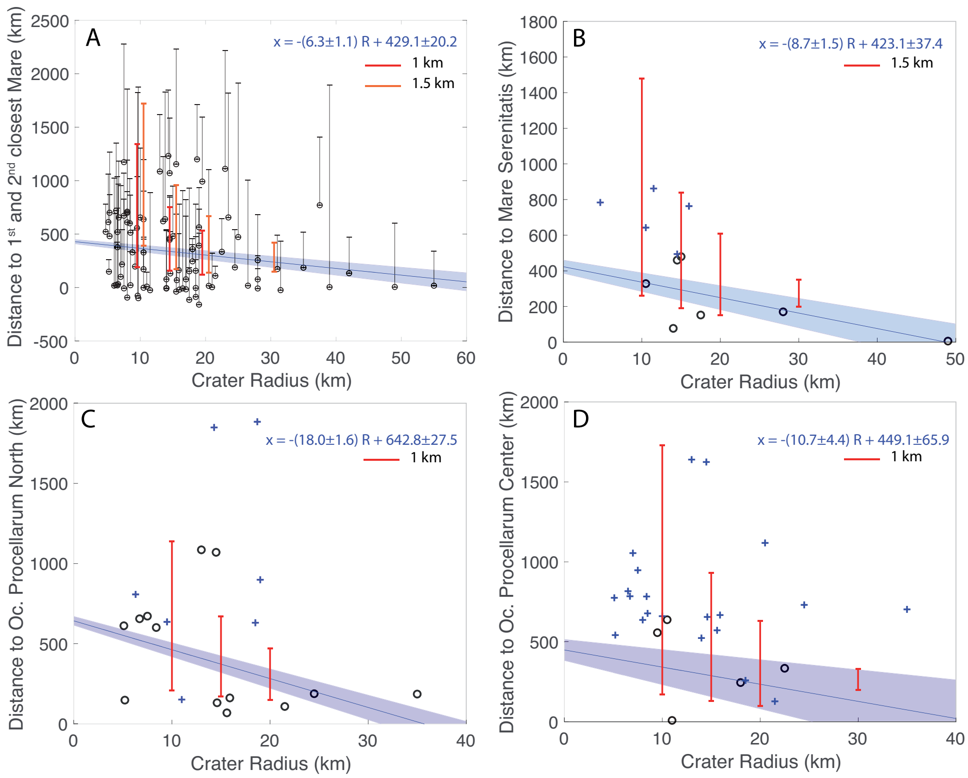


Figure 6: A: Distance from first (circle) and second (dash) closest mare for each floor fractured craters of Class 2, 3 and 4 (showing an elevated floor) as a function of crater radius. We assume circular maria of given radius and centre (Table 2). Thick lines indicate predicted distance range of FFCs of given radius from a load of radius $\tau_M = 350$ km and thickness 1 (red) or 1.5 km (orange). The linear regression line and equation fitting data corresponding to the closest mare are shown in blue, with the coloured area corresponding to the regression error for an error on the distance of $\pm 100$ km. B, C, D: Distance of closest FFCs from different maria as a function of FFCs radius. Black circles: FFCs for which the mare considered is the closest one, blue crosses: FFCs for which the mare considered is the second closest one. Predicted distance range are indicated as errorbars in red and the regression line (regression error is obtained considering an error on the distance of $\pm$ 50 km) and its equation fitting data corresponding to FFCs for which the Mare is the closest one (circles) are indicated in blue and coloured area. B: Mare Serenitatis, modelled as a cylindrical load of radius 300 km. Predicted distance ranges are for a load radius of 300 km and thickness 1.5 km. C: Northern part of OP, modelled as a cylindrical load of radius 300 km. Predicted distance ranges are for a load radius of 300 km and thickness 1 km. D: Central part of OP modelled as a load of radius 450 km. Predicted distance ranges are for a load radius of 450 km and thickness 1 km. Calculations use $E = 50$ GPa, $T_e = 70$ km, $D_c = 35$ km, $\nu = 0.2$, $g = 1.62$ ms$^{-2}$ and $\rho_L = 3400$ kg.m$^{-3}$

the height required for a vertical dike to turn into a sill. Using this approach we are able to drop the assumption that dikes instantaneously adjust to the direction favoured by the principal stresses. Dike trajectories are computed by maximising the strain plus gravitational energy released by the dike on incremental propagations along different test directions (Maccaferri et al., 2011). This calculation allows to track the actual dike trajectory which does not depend only on the local stress field but also on magma driving force and to check under which conditions a vertical dike starting from the base of the crust may get stacked as a horizontal sill at shallow depth beneath an impact crater. The BE model for dike propagation is fed with a radial cross section of the stress field acting within the crust beneath an impact crater, as computed with COMSOL (Figure 5). The horizontal stress component is given by $\sigma_\Theta^T$ and the vertical component is only induced by crater unloading.

We consider several specific favourable cases where the membrane stress component induced by mare loading dominates, producing azimuthal tensile stress and favouring radial dikes turning into sills. Vertical dykes start $10$ km below the crust, at 45 km depth, with a given volume and internal pressure, at different distances ($\mathrm{x}_C = 0.5, 1.0, 2.0, 30$ km) from the crater axis (Figure 7). Magma is assumed to be buoyant in the mantle but not in the crust (which is 35 km thick).

Although magma loses pressure in the crust, where it is negatively buoyant, its driving pressure allows for further ascent and the intrusion does not stop at the crust base. Simulations show that for larger magma volume and driving force, the dyke is less deviated from its vertical path and ascends farther up in the crust. Therefore, the transition from a dyke to a sill occurs at shallower depths than $H_s$. If the driving force is sufficiently large (Figure 7), the magma might even reach

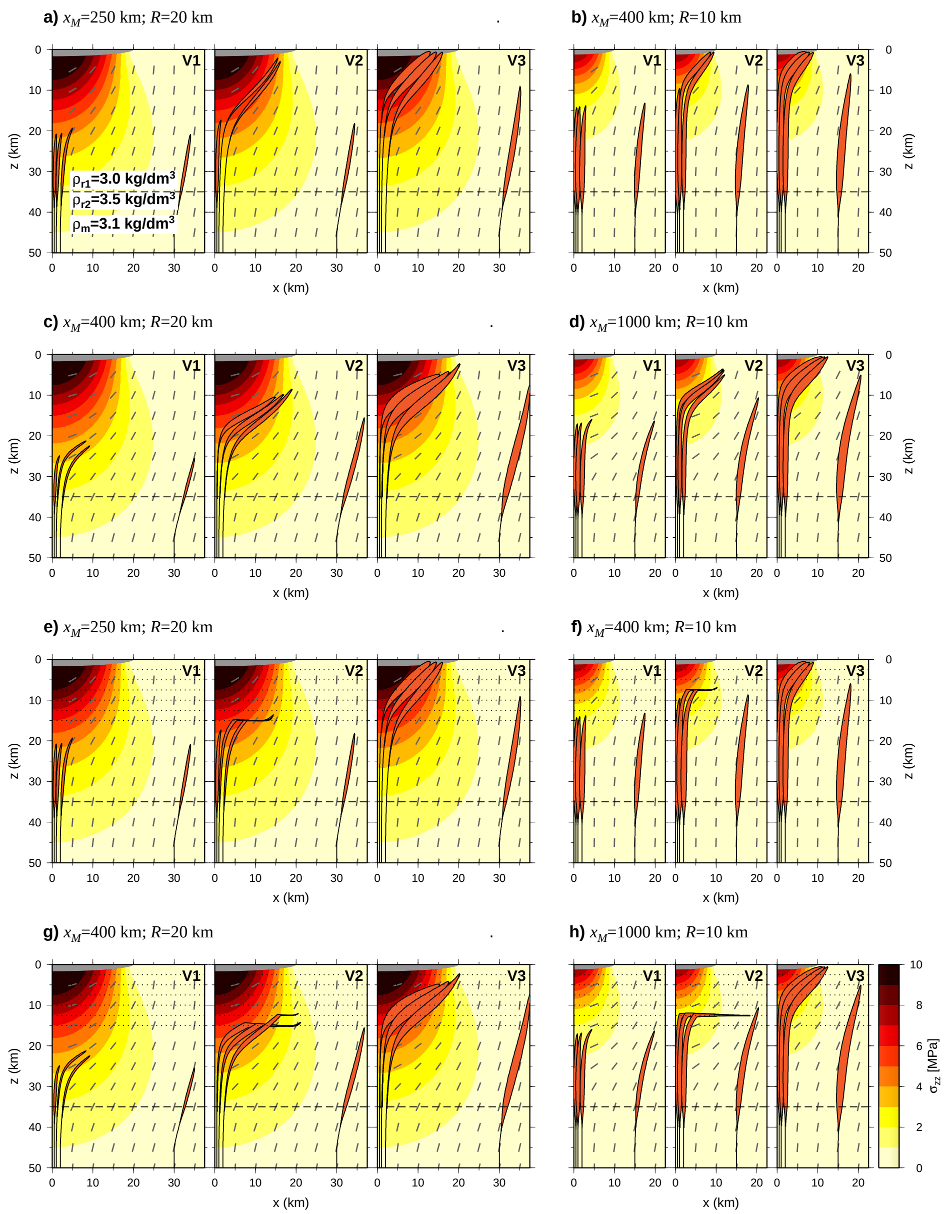


Figure 7: Panels 'a' to 'd') Simulated dike trajectories (red elongated sheet intrusions) for different stress scenarios, and different magma volumes (that is the dike cross section, in the 2D model: $V_3 = 0.25$ km$^2$, $V_2 = 0.5 \times V_3$, $V_1 = 0.5 \times V_2$). Panels 'e' to 'h') same simulations but including six weak layers (dotted lines) at regular depth intervals between 2.5 and 15 km depth. In all simulations dikes start at 45 km depth. $\rho_{r1}$, $\rho_M$, and $\rho_{r2}$ are the densities of crustal rocks, magma, and mantle rocks, respectively. The dashed horizontal line is the crust-mantle boundary. Grey dashes indicate the direction of $\sigma_1$. The intensity of the vertical component of loading and unloading stresses is plotted as colour contour. In panels a) and e) we consider the stress induced by a crater of radius $R = 20$ km at a distance $x_M = 250$ km from the load. b) and f) $R = 20$ km, $x_M = 400$ km. c) and g) $R = 10$ km, $x_M = 400$ km. d) and h) $R = 10$ km, $x_M = 1000$ km. We used $T_e = 70$ km, $\tau_M = 350$ km, $h_M = 4$ km, $E = 10$ GPa and $\nu = 0.2$.

the surface, as also shown by Michaut and Pinel (2018) for large craters on a thin crust. Far from the crater axis, the local crater stress field is negligible and the vertical dyke is not deviated. Dykes starting far away from a crater would also stagnate at deeper depths that the ones starting below the crater axis. This is due to the larger decrease in pressure as the intrusion ascends below the crater unloading (Michaut and Pinel, 2018).

Our calculations show that the depth of the dyke-to-sill transition is controlled by the magnitude of the deviatoric stress compared to magma driving force. The deviatoric stress below craters becomes significant at a depth similar to the crater radius (Figure 2). Hence, below small craters on a thick crust, if the magma intrusion starts as a vertical dyke, it can ascend up to shallow depths equivalent to the crater radius before being deviated (Figure 7). This confirms that the entire range of distances from the mare for which we expect FFCs, according to the calculations carried out is the previous section, indeed lead to shallow sill intrusions.

Finally, we test the effect of a weak layer interface on magma propagation, to reproduce the presence of a brecciated or fractured zone, which has been previously proposed as a possible cause for sill emplacement below impact craters (Schultz, 1976a; Jozwiak et al., 2012). Our simulations show that such a weak layer can help the process of horizontalization if the magma driving force is low enough (for a large volume or large driving pressure, the dyke path always remains unperturbed by the weak layer, see cases V3, bottom of Figure 7). However, in order for the dyke to intrude through the weak interface (characterised by null fracture toughness of the rocks), it is necessary to consider also the local stress field due to the crater unloading. In fact, dykes starting far from a crater, which are not directly affected by the crater unloading, does not intrude within the weak interface (Figure 7 panels f and h volume V2).

### *4.3. Effect of Young's modulus, crustal and elastic lithosphere thicknesses*

For a given elastic plate thickness $T_e$, crater unloading causes compression at depths $z \gtrsim 2T_e/3$ which inhibits magma ascent (Figure 3 in Michaut and Pinel (2018)). The presence of crater-centred intrusions below craters in region of crustal thickness of $\sim 30 - 40$ km (Figure 3 in Michaut and Pinel (2018)) thus argues for a relatively thick lithosphere such that $T_e \geq 70$ km at the time of magma ascent below craters. The Young's modulus value has a negligible effect on this estimate (in particular, Equation 3 does not depend on $E$).

As long as $D_c \lesssim 2T_e/3$, increasing the crustal thickness would increase the maximum distance from the mare at which FFCs can form. This is because a thicker crust would more easily allow for vertical dykes at its base, wherever the effect of mare loading dominates over crater unloading (Figure 2). The fact that the crust generally thickens farther from the mare (Wieczorek et al., 2013) thus favours the development of crater-centred intrusions far from the load.

For a given crustal thickness, crater and load radius, a thicker elastic lithosphere slightly increases the minimum load thickness necessary to meet the condition for FFCs formation. However, the effect of elastic thickness variations on possible distance range of FFCs from mare is negligible.

Young's modulus values are larger for mantle rocks than for crustal rocks and decrease with porosity and temperature (Pritchard and Stevenson, 2000) spanning a range between 10 and 100 GPa, with most studies considering values between 50 and 100 GPa for the lithosphere (Solomon and Head, 1979). The value of $E$ quite significantly affects our results: the larger $E$, the larger the amplitudes of both bending and membrane stresses due to mare loading are (see Appendix) and the wider the range of possible distances for FFCs from the load for given load properties (i.e. given $\tau_M$, $h_M$), (Figure 5). In the following, we consider a value of $50$ GPa and $T_e = 70$ km.

### 4.4. *Mare thicknesses*

The main maria have radii between $\sim 150$ and $450$ km (see Table 2).

Within this range of load radius, we can calculate the minimum thickness that is necessary for magma ascent up to the floor of a crater with radius of 10 km. For this calculation, we use both the minimum value of the azimuthal membrane stress, that occurs at a few hundreds of kilometers from the load (Figure 3 B and C), as well as the mean value over the distance range 100-700 km from the load, that is the range of distances over which most FFCs of radius $\sim 10$ km are observed (Figure 6 A).

Results show that, in order to have small uplifted FFCs ($\sim 10$ km in radius), at a distance between 100 to 700 km from a load with radius $> 250$ km, the load thickness must be smaller than $\sim$ 3 km (Figure 8). Smaller FFCs, of Class 4 in particular, show uplifted floors rather than flooded floors. These craters are observed around the largest maria, in particular OP, Mare Serenitatis and Mare Crisium. Given mare radius (see Table 2), we deduce that the mare thickness is on average less than $< 1.6$ km in OP in its central part, $< 2.3$ km in Mare Serenitatis and $< 3.4$ km in Mare Crisium.

Taken all together, the range of distances between all FFCs with an uplifted floors and their first and second closest mare is consistent with an average mare thickness of $\sim$1 to 1.5 km, assuming $\tau_M = 350$ km (Figure 6 A).

FFCs may be influenced by a set of stresses imposed by the presence of more than one mare. Here, we assume that a FFC is under the influence of a given mare

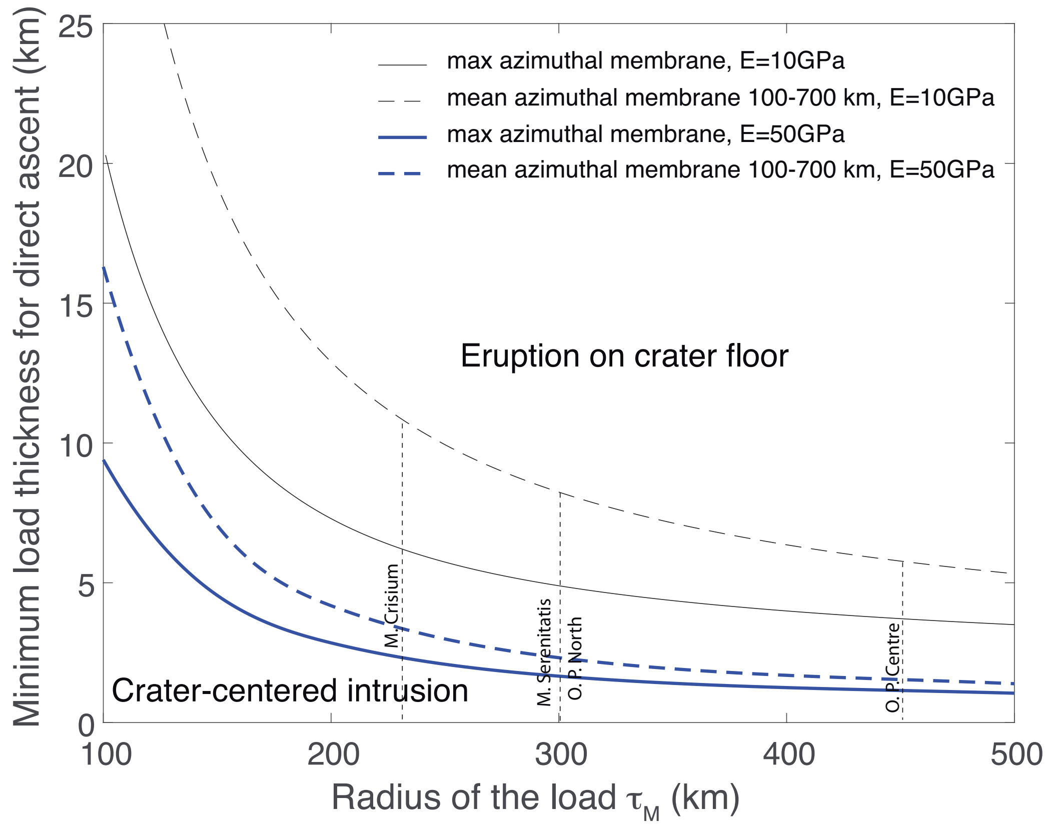


Figure 8: Load thickness $h_{asc}$ necessary for a direct ascent up to the crater surface for a crater radius of 10 km as function of load radius $\tau_M$. Dashed line: thickness calculated using the mean value of the azimuthal membrane stress between 100 and 700 km from the load. Solid line: thickness calculated using the maximum azimuthal membrane stress in tension (i.e. minimum value). Black lines: $E = 10$ GPa, blue lines, $E = 50$ GPa.

or mascon if this mare is the first or second closest mare to this crater. We observe that the distance range of FFCs from the mare indeed decreases as the FFC radius increases (Figure 6). In fact, a linear regression with significant negative slope fits FFCs radii versus their distance from the closest mare (Figure 6 B, C and D).

We found that FFCs distribution around OP are in general consistent with an average mare thickness of 1 km, in agreement with results from Gong et al. (2016), based on GRAIL's gravity data, but about twice the value proposed by De Hon (1979). However, the method used by De Hon (1979) only provides lower bounds on basalt thicknesses (Gong et al., 2016) and these authors also noted local lenses in excess of 1000-1500 m which increases the average load thickness.

The distribution of FFCs around Mare Serenitatis is consistent with a load thickness of $\sim$ 1.5 km for a load radius of 300 km. This estimate is in good agreement with Michaut et al. (2016) who found a thickness larger than 1.3 km and with the estimation of 1.6 km based on the deepest reflector detected by the Lunar Sounder Experiment (Peeples et al., 1978). East of Mare Serenitatis, Weider et al. (2010) estimated the thickness of 6 different layers, for a total of about 1500 m, also consistent with this study.

Evans et al. (2016) interpreted circular gravity anomalies lacking topographic expressions as flooded craters. By estimating their initial rim height, they obtained thicknesses larger than 1.5 km. Their study also point to local basalt lenses in excess of 7 km thickness. It appears quite logical that our regional-scale study fits better with their average value. We notice that our FFCs are generally observed closer to mare than what is expected from our model (Figures 6 and 8). Such a discrepancy might be explained by the thickening of the load towards the center of the mare, which is not considered in our simplified loading model.

## 5. Discussion and conclusion

Recently, Michaut and Pinel (2018) have shown that crater unloading may have triggered magma ascent within the lunar crust below mare-filled and floor-fractured craters. For large craters, the unloading was large enough to cause magma eruption on the crater floor. For small craters, the crater unloading was not large enough to cause an eruption and resulted in an intrusion. In that case, the magma driving pressure is small and the magma path is likely sensitive to the lithospheric stress state. Here we demonstrate that flow horizontalization, leading to sill-like intrusions below FFCs, was caused by the local stress state below crater unloading with a vertical least compressive stress favouring the emplacement of horizontal intrusions. The presence of a highly fractured, brecciated zone caused by the impact over a depth proportional to the crater size and possibly capped by impact-generated solidified melt (Schultz, 1976a; Wichman and Schultz, 1995), that we modelled as a weak layer interface below the crater, could have helped, but did not cause, the horizontalization of magmatic intrusions.

Furthermore, a tensional stress is necessary to explain horizontal spreading at shallow depth and crater floor uplift at FFCs. Mare and mascons loading on the lithosphere caused tensional membrane stresses in the azimuthal direction for a circular mare at their periphery over distances larger than $\sim 1000$ km favouring radial dyke opening. We demonstrate that the size and spatial distribution of FFCs of Class 2, 3 and 4, with the smaller FFCs being the farther away from the mare, is consistent with magma path below craters being controlled by the lithospheric state of stress, sum of the local stress due to crater unloading and of a regional horizontal pre-existing stress caused by mare loading. The distribution of FFCs around lunar maria is consistent with elastic lithosphere thicknesses $\geq 70$ km and average mare thicknesses $< 4$ km, in particular of $\sim 1$ km in OP using $E = 50$ GPa.

The conditions for which magma may accumulate as horizontal sills at shallow depths ($z \leq 10$ km) below impact craters are likely met below small craters ($R \leq 10$ km) surrounding mascons and maria. Indeed, the smaller the crater, the smaller the required additional pre-existing extension to obtain a vertical $\sigma_1$ at depth ensuring the ascent of magma to shallower depths. It is thus likely that the mechanism we propose is also the cause of the formation of lunar concentric craters (Trang et al., 2016). These craters, that have diameters commonly $< 15$ km, present anomalously shallow floors and a concentric ridge; they share the same distribution, surrounding the maria, as floor-fractured craters and probably result from crater-centred intrusions (Trang et al., 2016; Schultz, 1976b).

Here, we assume that the stress field seen by ascending magma is the summation of the regional mare-controlled stress before impact and of the unloading stress associated with crater topography. However, material fluidization caused by impact could reset the stress state in the crater subsurface, losing the memory of prior regional stress within an hemisphere of radius $\sim R$. In that case, once the crater motion ceases, the elastic medium still has to compensate for the final crater topography, and unloading forces would still dominate the local stress, promoting shallow sill formation (vertical $\sigma_3$). As the stress will not be discontinuous after the impact and the regional stress is still present at depths $> R$, the resulting stress at shallower depths should be equivalent to a reduced regional stress field in addition to the local crater stress field. In that case, our mare thickness estimates would provide a lower bound.

On Earth, radial dike swarms have been used to characterise local stress perturbations induced either by the magmatic plumbing system (Odé, 1957; Muller and Pollard, 1977; Mériaux and Lister, 2002) or the volcanic edifice (Roman and Jaupart, 2014). Lessons learned from Earth applied volcanology have been transferred to planetology with success. In particular, similar giant dike swarms observed on Venus have been interpreted either in terms of local plumbing system or large scale rising diapir effects (Ernst et al., 1995; Galgana et al., 2013). More recent studies of magma transport on Earth have relied not only on the magmatic intrusion shape and orientation but also on vent location to gain quantitative information on the stress state, otherwise difficult to constrain, within volcanic edifices (Maccaferri et al., 2017) or rifting areas (Maccaferri et al., 2014). In particular, the surface unloading effect induced by caldera formation has been proven to strongly affects the magma trajectory favouring horizontal deflection at shallow depth and sill-shaped storage zone formation (Corbi et al., 2015). The present study shows that applying these new concepts, based on magma ability to reach the surface and on the path followed by magma in the crust, to planetary volcanism, opens new perspectives. Additional information on the lithospheric elastic thickness (see Michaut and Pinel (2018) as well as this study) and on its state of stress can be derived. Conversely, applications of magma transport models on various terrestrial planets and settings improve their validation to larger parameters ranges.

## Acknowledgments

This work has been realised thanks to the financial support of the IDEXLyon Project of the University of Lyon in the frame of the ”Programme Investissements d’Avenir” (ANR-16-IDEX-0005), PNP/INSU/CNES, as well as the Région Auvergne Rhône-Alpes. The collaboration between ISTerre and GFZ was funded by the Campus France-DAAD exchange program and the ANR-DFG NLE 2018 MagmaPropagator projet (ANR-18-CE92-0037). The authors thank the editor W. McKinnon and two anonymous reviewers for their help in improving our manuscript.

## Appendix A. Stress due to a cylindrical load on an elastic shell

We use the analytical solution by Brotchie (1971), also used by Solomon and Head (1979) and Freed et al. (2001) to calculate the stress in a spherical elastic shell of thickness $T_e$, Young's modulus $E$, Poisson's ratio $\nu$ due to a cylindrical load of radius $\tau_M$, thickness $h_M$, density $\rho_M$. The shell overlies a fluid of density $\rho_L$. We note $q_M = \rho_M g h_M$ and the flexural rigidity $D = ET_e^3/(12(1-\nu^2))$. We note the radius of ”relative stiffness” $L$

$$L = \left( \frac{D}{ET_e/R^2 + \rho_L g} \right)^{1/4} \tag{A.1}$$

We also note $d_M = \tau_M/L$ and $x = \tau_M + \mathrm{x}_M$, and $R_s$ the spherical radius to the midplane of the shell. Outside the load ($\mathrm{x}_M > 0$), the vertical displacement $w$, positive downwards, the radial and azimuthal moment $M_\Phi$ and $M_\Theta$ and radial and azimuthal resultant $N_\Phi$ and $N_\Theta$ are :

$$w = \frac{q_M d_M}{ET_e/R_s^2 + \rho_L g} \left(\mathrm{Ber}'\, d_M \,\mathrm{Ker}\, x \; - \mathrm{Bei}'\, d_M \,\mathrm{Kei}\, x\right) \tag{A.2}$$

$$M_\Phi = -q_M d_M L^2 \left[\mathrm{Ber}'\, d_M \left(\mathrm{Kei}\, x + \frac{1-\nu}{x}\,\mathrm{Ker}'\, x\right) + \mathrm{Bei}'\, d_M \left(\mathrm{Ker}\, x - \frac{1-\nu}{x}\,\mathrm{Kei}'\, x\right)\right] \tag{A.3}$$

$$M_\Theta = -q_M d_M L^2 \left[\mathrm{Ber}'\, d_M \left(\nu\,\mathrm{Kei}\, x - \frac{1-\nu}{x}\,\mathrm{Ker}'\, x\right) + \mathrm{Bei}'\, d_M \left(\nu\,\mathrm{Ker}\, x + \frac{1-\nu}{x}\,\mathrm{Kei}'\, x\right)\right] \tag{A.4}$$

$$N_\Phi = \frac{q_M E T_e/R_s}{ET_e/R_s^2 + \rho_L g} \left[\frac{1}{2}\frac{d_M^2}{x^2} + \frac{d_M}{x}\left(\mathrm{Ber}'\, d_M \,\mathrm{Kei}'\, x + \mathrm{Bei}'\, d_M \,\mathrm{Ker}'\, x\right)\right] \tag{A.5}$$

$$N_\Theta = -N_\Phi + ET_e w/R_s \tag{A.6}$$

where Ber, Bei, Ker and Kei are Bessel-Kelvin functions of order zero and the prime denotes their first derivatives.

Within the shell at $(R_s - T_e/2) \leq r \leq (R_s + T_e/2)$, the net horizontal radial stress $\sigma_\Phi$ and azimuthal stress $\sigma_\Theta$ with respect to lead center are:

$$\sigma_\Phi = -\frac{N_\Phi}{T_e} + \frac{12 M_\Phi}{Te^3}(r - R_s) \tag{A.7}$$

$$\sigma_\Theta = -\frac{N_\Theta}{T_e} + \frac{12 M_\Theta}{Te^3}(r - R_s) \tag{A.8}$$

## References


Anderson, E. M., 1951. The dynamics of faulting and dyke formation with applications to Brittan, Edinburgh. London, Oliver and Boyd.

Brotchie, J. F., 1971. Flexure of a liquid-filled spherical shell in a radial gravity field. Modern Geol. 3, 15–23.

Cartwright, J., Moller Hansen, D., 2006. Magma transport through the crust via interconnected sill complexes. Geol. Soc. Am. Bull. 34, 929–932.

Corbi, F., Rivalta, E., Pinel, V., Maccaferri, F., Acocella, V., 2016. Understanding the link between circumferential dikes and eruptive fissures around calderas based on numerical and analog models. Geophysical Research Letters 43 (12), 6,212–6,219.

Corbi, F., Rivalta, E., Pinel, V., Maccaferri, F., Bagnardi, M., Acocella, V., 2015. How caldera collapse shapes the shallow emplacement and transfer of magma in active volcanoes. Earth and Planetary Science Letters 431, 287 – 293.

De Hon, R. A., 1979. Thickness of western mare basalts. Proc. Lunar Planet. Sci. Conf. 10, 2,935–2,955.

Ernst, R., Head, J. W., Parfitt, E., Grosfils, E., 1995. Giant radiating dyke swarms on Earth and Venus. Earth Sci. Rev. 39, 1–58.

Evans, R., Soderblom, J. M., Andrews-Hanna, J. C., Solomon, S. C., Zuber, M. T., 2016. Identification of buried lunar impact craters from GRAIL data and implications for the nearside maria. Geophys. Res. Lett. 43, 2,445–2,455.

Freed, A. M., Melosh, H. J., Solomon, S. C., 2001. Tectonics of mascon loading: Resolution of the strike-slip faulting paradox. J. Geophys. Res. (Planets) 106, 20,603–20,620.

Galgana, G. A., Grosfils, E. B., McGovern, P. J., 2013. Radial dike formation on Venus: Insights from models of uplift, flexure and magmatism. Icarus 225, 538–547.

Gong, S., Wieczorek, M. A., Nimmo, F., Kiefer, W. S., Head, J. W., Huang, C., Smith, D. E., Zuber, M. T., 2016. Thicknesses of mare basalts on the Moon from gravity and topography. J. Geophys. Res. (Planets) 121, 854–870.

Jozwiak, L. M., Head, J. W., Wilson, L., 2015. Lunar floor-fractured craters as magmatic intrusions: Geometry, modes of emplacement, associated tectonic and volcanic features, and implications for gravity anomalies. Icarus 248, 424–447.

Jozwiak, L. M., Head, J. W., Zuber, M. T., Smith, D. E., Neumann, G. A., 2012. Lunar floor-fractured craters: Classification, distribution, origin and implications for magmatism and shallow crustal structure. J. Geophys. Res. (Planets) 117, 10.1029/2012JE004134.

Laneuville, M., Wieczorek, M. A., Breuer, D., Tosi, N., 2013. Asymmetric thermal evolution of the Moon. J. Geophys. Res. 118, 1,435–1,452.

Maccaferri, F., Bonafede, M., Rivalta, E., 2011. A quantitative study of the mechanisms governing dike propagation, dike arrest and sill formation. J. Volcanol. Geotherm. Res. 208, 39–50.

Maccaferri, F., Richeter, N., Walter, T. R., 2017. The effect of giant lateral collapses on magma pathways and the location of volcanism. Nature Communications 8, 10.1038/S41467-017-01256-2.

Maccaferri, F., Rivalta, E., Keir, D., Acocella, V., 2014. Off-rift volcanism in rift zones determined by crustal unloading. Nature Geoscience 7, 297–300.

McGovern, P. J., Litherland, M. M., 2011. Lithospheric stress and basaltic magma ascent on the Moon, with implications for large volcanic provinces and edifices. 42nd LPSC Abstract, 2,587.

Melosh, J., 1976. On the origin of fractures radial to lunar basins. Proc. Lunar Sci. Conf. 7th, 2,967–2,982.

Menand, T., 2011. Physical controls and depth of emplacement of igneous bodies: A review. Tectonophysics 500, 11–19.

Menand, T., Daniels, K. A., Benghiat, P., 2010. Dyke propagation and sill formation in a compressive tectonic environment. J. Geophys. Res. 115, 10.1029/2009JB006791.

Mériaux, C., Lister, J. R., 2002. Calculation of dike trajectories from volcanic centres. J. Geophys. Res. 107(B4), 1–10.

Michaut, C., Pinel, V., 2018. Magma ascent and eruption triggered by cratering on the Moon. Geophys. Res. Lett. 45, 10.1029/2018GL078150.

Michaut, C., Thiriet, M., Thorey, C., 2016. Insights into mare basalt thicknesses on the Moon from intrusive magmatism. Phys. Earth Planet. Int. 257, 187–192.

Muirhead, J. D., Airoldi, G., Rowland, J. V., Connor, L., White, J. D. L., 2012. Interconnected sills and inclined sheet intrusions control shallow magma transport in the Ferrar large igneous province, Antarctica. Geol. Soc. Am. Bull. 124, 162–180.

Muller, O. H., Pollard, D. D., 1977. The stress state near Spanisk Peaks, Colorado, determined from a dike pattern. Pure Appl. Geophys. 115, 69–86.

Nakamura, K., 1977. Volcanoes as possible indicators of tectonic stress orientation - principle and proposal. J. Volc. Geotherm. Res. 2, 1–16.

Neumann, G. A., Zuber, M. T., Wieczorek, M. A., McGovern, P. J., Baker, D. M. H., Solomon, S. C., Smith, D. E., Lemoine, F. G., Mazarico, E., Sabaka, T. J., Goossens, S. J., Melosh, H. J., Phillips, R. J., Asmar, S. W., Konopliv, A. S., Williams, J. G., Sori, M. M., Soderblom, J. M., Miljkovic, K., Andrews-Hanna, J. C., Nimmo, F., Kiefer, W. S., 2015. Lunar impact basins revealed by gravity recovery and interior laboratory measurements. Sci. Adv. 1, 10.1126/sciadv.1500852.

Odé, H., 1957. Mechanical analysis of the dike pattern of the Spanish Peaks area, Colorado. Geol. Soc. Am. Bull. 68, 567–576.

Peeples, W. J., Sill, W. R., May, T. W., Ward, S. H., Philips, R. J., Jordan, R. L., Abbott, E. A., Killpack, T. J., 1978. Orbital radar evidence for lunar subsurface layering in Maria Serenitatis and Crisium. J. Geophys. Res. 83, 3,459–3,468.

Pinel, V., Carrara, A., Maccaferri, F., Rivalta, E., Corbi, F., 2017. A two-step model for dynamical dike propagation in two-dimensions: Application to the July 2001 Etna eruption. Journal of Geophysical Research: Solid Earth, 10.1002/2016JB013630.

Pinel, V., Jaupart, C., 2000. The effect of edifice load on magma ascent beneath a volcano. Phil. Trans. Roy. Soc. Lond. 358, 1,515–1,532.

Pritchard, M., Stevenson, D. J., 2000. Thermal aspects of lunar origin. In: Origin of the Earth and Moon. Tucson, Univ. of Arizona Press, pp. 179–196.

Richardson, J. A., Connor, C., Wetmore, P., Connor, L., Gallant, E., 2015. Role of sills in the development of volcanic fields: Insights from lidar mapping surveys of the San Rafael Swell, Utah. Geology 43, 10.1130/G37094.1.

Roman, A., Jaupart, C., 2014. The impact of a volcanic edifice on intrusive and eruptive activity. Earth Planet. Sc. Lett. 408, 1–8.

Schultz, P. H., 1976a. Floor-fractured lunar craters. Moon 15, 241–273.

Schultz, P. H., 1976b. Moon morphology: Interpretations based on lunar orbiter photography. University of Texas Press, Austin, Texas, p. 626.

Sneddon, I. N., 1951. Fourier Transforms. Dover Publications, New York.

Solomon, S. C., Head, J. W., 1979. Vertical movement in mare basins: Relation to mare emplacement, basin tectonics, and lunar thermal history. J. Geophys. Res. (Planets) 84, 1,667–1,682.

Thomas, R. J., Rothery, D. A., Conway, S. J., Anand, M., 2015. Explosive volcanism in complex impact craters on Mercury and the Moon: Influence of tectonic regime on depth of magmatic intrusion. Earth Planet. Sc. Lett. 431, 164–172.

Thorey, C., Michaut, C., 2014. A model for the dynamics of crater-centered intrusions: application to lunar floor-fractured craters. J. Geophys. Res. (Planets) 119, 286–312.

Thorey, C., Michaut, C., Wieczorek, M., 2015. Gravitational signatures of lunar floor-fractured craters. Earth Planet. Sc. Lett. 424, 269–279.

Trang, D., Gillis-Davis, J. J., Hawke, B. R., 2016. The origin of lunar concentric craters. Icarus 278, 62–78.

Watanabe, T., Masuyama, T., Nagaoka, K., Tahara, T., 2002. Analog experiments on magma-filled cracks: Competition between external stresses and internal pressure. Earth, Planets, Space 54, 1247–1261.

Weider, S. Z., Crawford, I. A., Joy, K. H., 2010. Individual lava flow thicknesses in Oceanus Procellarum and Mare Serenitatis determined from Clementine multi-spectral data. Icarus 209, 323–336.

Wichman, R. W., Schultz, P. H., 1995. Floor-fractured craters in Mare Smythii and West of Oceanus Procellarum implications of crater modification by viscous relaxation and igneous intrusion models. J. Geophys. Res. (Planets) 100, 21,209–21,218.

Wieczorek, M. A., Neumann, G. A., Nimmo, F., Kiefer, W. S., Taylor, G. J., Melosh, H. J., Phillips, R. J., Solomon, S. C., Andrews-Hanna, J. C., Asmar, S. W., Konopliv, A. S., Lemoine, F. G., Smith, D. E., Watkins, M. M., Williams, J. G., Zuber, M. T., 2013. The crust of the Moon as seen by GRAIL. Science 339, 671–675.

Wilson, L., Head, J. W., 2017. Generation, ascent and eruption of magma on the Moon: New insights into source depths, magma supply, intrusions and effusive/explosive eruptions (Part 1: Theory). Icarus 283, 146–175.

Wood, J. A., Dickey, J. S., Marvin, U. B., Powell, B. N., 1970. Lunar anorthosites and a geophysical model of the Moon. Proc. Apollo 11 Lunar Sci. Conf., 1965–1988.

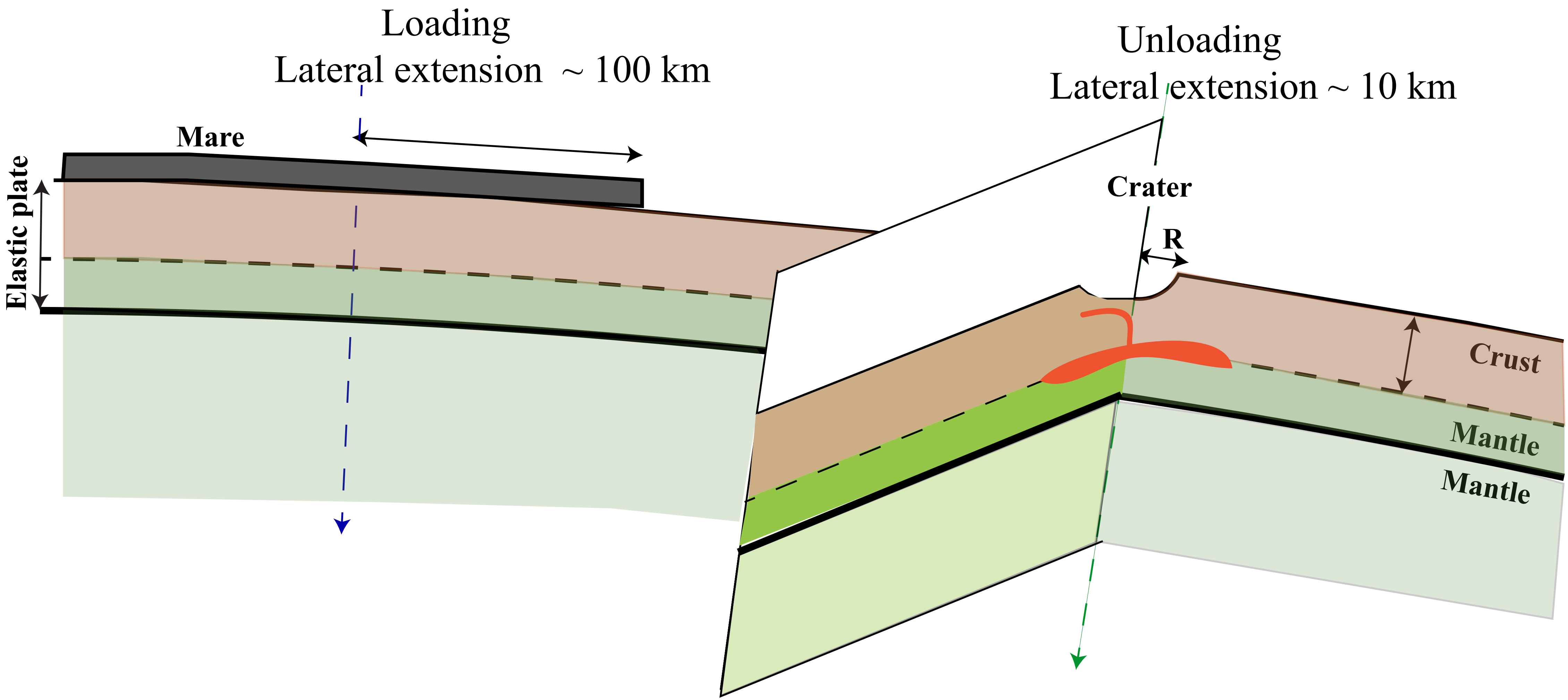
Loading
Lateral extension ~ 100 km
Unloading
Lateral extension ~ 10 km
Mare
Elastic plate
Crater
R
Crust
Mantle
Mantle